Applied Physics Letters

Resonance-regulated stick-slip locomotion in a dual-soft-legged vibratory robot

Jingyuan Zeng,[1] Ke Huang,[1] Zitong Zeng,[1] and Jiaying Zhang[1]
School of Aeronautic Science and Engineering, Beihang University, Beijing 100191, China

(*Electronic mail: jiaying.zhang@buaa.edu.cn)

(Dated: 25 September 2026)

Inspired by the bristle-like anisotropic structures of foxtail grass, this letter presents a dual-soft-legged vibratory robot that exploits frictional anisotropy to generate directed locomotion driven by a single eccentric motor. The interaction among structural deformation, eccentric inertial excitation, and tangential friction enables transitions among multiple locomotion states. A reduced dynamic model is then developed to couple forward translation, heave, and pitch rotation with Coulomb friction under unilateral contact. Numerical simulations identify different locomotion states governed by soft-leg stiffness and excitation frequency, including stationary, slow-forward, intermittent, transitional, and high-speed forward states. Experiments validate the results and show that the measured displacement arises from repeated stick–slip transitions. An implicit critical equation derived from the simplified dynamic model captures the onset boundary between stationary and moving states, while the resonance curves closely align with the characteristic regions in the numerical state map. This agreement reveals that locomotion emerges from the interaction among eccentric inertial forcing, dynamically modulated friction thresholds, and resonant structural response. This work establishes a physical framework for friction-driven vibration mechanism and provides insight into the use of structural resonance for tunable stick–slip locomotion.

Frictional regulation is a central mechanism for locomotion in both biological and engineered systems. Organisms such as geckos, caterpillars, and mayfly larvae exploit structured contacts, body deformation, or anisotropic interfacial forces to regulate adhesion and propulsion. Autumn et al.[1–4] studied the epidermal bristle structures of geckos and lizards. They found that van der Waals forces between bristle and contact surfaces, along with the resulting friction, are key to adhesion. Plaut et al.[5,6] analyzed the locomotion behavior of inchworms. They explored how inchworms regulate friction through body deformation. Petra et al.[7–10] studied the gill structures of mayfly larvae. They found that the interaction between gills and pebbles effectively reduces the impact of water flow. In summary, such structural adaptability effectively regulates frictional interactions with contacted objects, which holds great potential for micro-robot applications. Therefore, extensive research on bio-inspired functional structures has widely investigated[11–15].

Frictional anisotropy in bio-inspired functional structures has attracted considerable attention[16–18]. Some studies show that asymmetry and rigidity of surface structures have the main influence on frictional anisotropy[19,20], which provide a broad foundation for fabricating structures with friction-induced anisotropy[20–23]. Meanwhile, soft-legged robots based on this principle have drawn much interest due to their diverse locomotion modes and complex mechanisms. Yan et al.[24] proposed a vibratory robot with an array of soft legs. Through vibration driving and multi-leg coordination, it achieved efficient locomotion on complex terrain. Meng et al.[25] established a mechanical model for a vibratory robot with a soft-leg array. They analyzed the triggering conditions and mechanisms of sliding and jumping modes, which provided guidance for stiffness design and terrain adaptation of soft-legged robots.

Barois et al.[26] combined mechanical resonance with the nonlinearity of stick-slip friction. This enabled direction-controllable locomotion of soft structures on a vibrating platform. Iyobe et al.[27] developed a single-motor-driven soft-bodied vibration robot based on two-dimensional repetitive slit patterns (2DRSPs), in which the body stiffness distribution was designed to tune resonant vibration modes. By changing the motor vibration frequency, different resonant modes were selectively excited, allowing the robot to switch among rotation and forward/backward locomotion modes. However, these studies mainly focused on single soft bodies, minimal soft structures, or systems with a limited number of contact elements; the locomotion-state selection and transition mechanisms in mechanically coupled multi-leg soft systems remain insufficiently resolved. Liu et al.[28] and Iyobe et al.[27] demonstrated that locomotion responses can be regulated by excitation parameters, frictional asymmetry, and structural resonance. Additionally, stick-slip transition has been widely recognized as a threshold frictional instability governing the onset of sliding and friction-mediated motion[29]. However, the coupled dynamics among structural vibration, multi-point frictional contact, and collective leg motion have not yet been systematically clarified.

Foxtail grass is a common plant in nature whose inclined bristle-like structures produce anisotropic frictional interactions with contacting surfaces. When placed on a vibrating platform, foxtail grass exhibits repeatable directional motion, reflecting the frictional anisotropy associated with its inclined bristle morphology, as shown in Figure 1(a,b). Inspired by this bio-inspired frictional mechanism, this letter introduces a dual-soft-legged vibratory robot driven by a single eccentric motor to study friction-regulated stick–slip locomotion. Figure 1(c) shows the robot prototype, which consists of two soft legs oriented in the same direction to generate asymmetric tangential friction. By varying the soft-leg stiffness and excitation frequency, the robot can transition among distinct locomotion states. A theoretical dynamic model is established to describe the coupling among forward translation, heave,

pitch rotation, and Coulomb friction under unilateral contact, as shown in Figure 1(d). Numerical and experimental results demonstrate that the robot exhibits multiple locomotion states governed by soft-leg stiffness and excitation frequency. Furthermore, the implicit onset criterion and the agreement between resonance curves and the numerical state map reveal the mechanism underlying the transition between stationary and moving states.

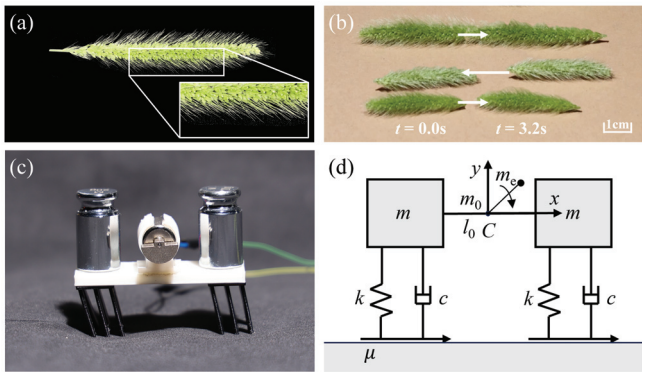


FIG. 1: Bio-inspired design of the dual-soft-legged vibratory robot based on the anisotropic bristle structure of foxtail grass. (a) Inclined bristle-like morphology of foxtail grass. (b) Vibration-induced directional locomotion of foxtail grass on a vibrating platform. (c) Bio-inspired robot prototype. (d) Reduced dynamic model. Multimedia available online.

This letter models the dual-soft-legged vibratory system as the reduced dynamic model shown in Figure 1(d). It consists of two identical mass-spring-damper systems, a connecting plate, and an eccentric motor, the eccentric inertial excitation induces structural deformation, modulates the normal contact force, and changes the instantaneous friction threshold, thereby producing tangential stick–slip locomotion. Here, m denotes the mass of each mass block. l_0 and m_0 denote the length and mass of the connecting plate, respectively. A_e, m_e, and ω denote the eccentricity, eccentric mass, and rotational frequency of the eccentric motor, respectively. k and c denote the spring stiffness and damping coefficient, respectively. μ denotes the friction coefficient between the soft legs and the ground during rightward motion.

For simplicity, several assumptions are introduced: the connecting plate is modeled as rigid; the tangential friction follows Coulomb's friction law[30]; the spring and damper remain perpendicular to the ground at all times; the mass of the spring-damper system is negligible compared to the total mass; the backward friction coefficient is assumed to be sufficiently large compared with the forward friction coefficient[16].

The forward displacement x, heave displacement y, and pitch rotation of the plate center θ are introduced to describe three generalized coordinates: forward translation, heave, and pitch rotation about the plate center C. For x, the rightward direction is defined as positive. For y, the upward direction is defined as positive. In the right-hand coordinate system, the counterclockwise direction is defined as positive for θ. At the initial moment, the eccentric block of the motor starts rotating clockwise from the top position. All coordinates are zero. The springs are at their natural lengths. The connecting plate is horizontal. The left and right mass blocks are labeled as blocks 1 and 2, respectively.

The dynamic equations of the system are established using the Lagrange equation (Appendix A)

$$\begin{aligned}(2m+m_0+m_e)\ddot{x}-m_eA_e\ddot{\theta}\cos(\omega t-\theta)-\\ m_eA_e(\omega-\dot{\theta})^2\sin(\omega t-\theta)=2\mu(ky+c\dot{y}),\end{aligned} \tag{1}$$

$$\begin{aligned}(2m+m_0+m_e)\ddot{y}+m_eA_e\ddot{\theta}\sin(\omega t-\theta)-\\ m_eA_e(\omega-\dot{\theta})^2\cos(\omega t-\theta)+\\ (2m+m_0+m_e)g+2ky+2c\dot{y}=0,\end{aligned} \tag{2}$$

$$\begin{aligned}\left(\frac{ml_0^2}{2}+\frac{m_0l_0^2}{12}\right)\ddot{\theta}+m_eA_e^2\ddot{\theta}-m_e\ddot{x}A_e\cos(\omega t-\theta)+\\ m_e\ddot{y}A_e\sin(\omega t-\theta)+m_egA_e\sin(\omega t-\theta)+\\ \frac{kl_0^2\sin(2\theta)}{4}+\frac{cl_0^2\dot{\theta}}{4}(\cos 2\theta+1)=-2\mu y(ky+c\dot{y}).\end{aligned} \tag{3}$$

Since the contact between the soft legs and the ground is a unilateral constraint, whether each soft leg contacts the ground must be discussed. As the eccentric motor rotates, the eccentric force excites the system to vibrate. The normal force changes accordingly, which further alters the maximum static friction the system can produce. Forward slip occurs when the horizontal component of the eccentric inertial force exceeds this instantaneous friction threshold. The detailed numerical calculation flowchart is given in Appendix B. Two motion states are distinguished in this procedure. In the sliding state both soft legs remain in contact with the ground, so the normal contact force of each leg is positive, the friction threshold varies with the instantaneous normal force, and forward slip occurs whenever the horizontal component of the eccentric inertial force exceeds this threshold. The stepwise displacement response discussed below is the result of these repeated crossings. In the jumping state the normal contact force of a soft leg vanishes and that leg leaves the ground, so the stiffness and damping contributions of the airborne leg are removed from the corresponding equations and the motion is governed by the contact state of the remaining leg, as described in Appendix B. For the parameters used in the main text the system is essentially in the sliding state; the jumping state occurs at higher excitation frequencies or in the resonance region. The dynamic equations are solved numerically using MATLAB.

Using the system parameters listed in Table I, the simulated horizontal displacement response is obtained, as shown in Figure 2(b). Over a long time scale, the displacement exhibits an almost linear forward drift. A magnified view reveals discrete slip jumps separated by sticking intervals, indicating that the apparent continuous drift results from accumulated stick-slip events.

To validate the model, a dual-soft-legged vibratory robot with parameters consistent with Table I was fabricated, as

TABLE I: Model parameters

Parameter	Value	Unit
Mass of each mass block m	0.022	kg
Mass of connecting plate m_0	0.0155	kg
Mass of eccentric block m_e	0.0026	kg
Length of connecting plate l_0	0.05	m
Eccentricity (amplitude) A_e	0.002	m
Equivalent damping coefficient of legs c	0.8	$N \cdot s/m$
Equivalent stiffness coefficient of legs k	450	N/m
Angular frequency of motor ω	278.65	rad/s
Friction coefficient for forward motion μ	0.37	
Gravitational acceleration g	9.81	m/s^2

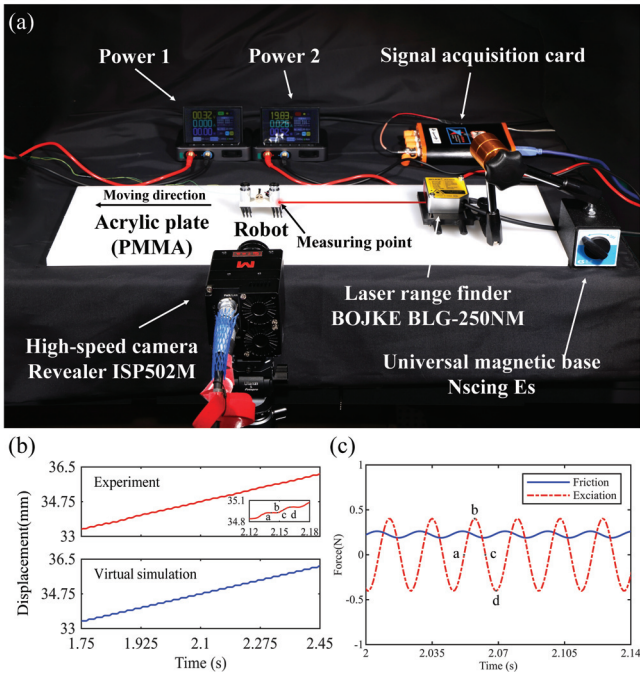


FIG. 2: Model validation and stick–slip mechanism. (a) Experimental setup for high-speed imaging and laser displacement measurement. (b) Simulated and measured horizontal displacement responses with a magnified stick–slip cycle. (c) Horizontal inertial force and instantaneous friction threshold, with points a–d indicating the characteristic instants.

shown in Figure 2(a). A high-speed camera (Revealer ISP502M, 1000fps, 1080p) was used to record the locomotion behavior. The robot's base plate was made of Bambu PLA Basic, and the brushes were made of Bambu TPU95A HF. The fabrication machine was Bambu H2D. The brushes were bonded to the base plate using double-sided tape. The robot was driven by a coreless motor with an eccentric block. The substrate for experiments was an acrylic (PMMA) plate.

The methods for measuring soft-leg stiffness and kinetic friction coefficient are given in Appendix C. A stick-slip phenomenon of intermittent motion was observed. A laser range finder was used to record the distance between one side of the robot and the sensor over time. This yielded the horizontal displacement curve of the robot. The experimental setup is shown in Figure 2(a). The stick-slip effect during robot locomotion is clearly visible. A comparison with the simulation results is shown in Figure 2(b). The measured displacement exhibits the same stepwise stick–slip phenomenon as the simulation, supporting the simplified dynamic model.

To further explore the mechanical mechanism behind the stick-slip phenomenon, a horizontal force analysis of the system is performed. The horizontal inertial force on the system is denoted as $m_e A_e(\omega-\dot{\theta})^2\sin(\omega t-\theta)$. The instantaneous friction threshold the ground can provide equals the product of the kinetic friction coefficient and the current normal force. Both are plotted in the same figure, as shown in Figure 2(c). The robot remains in the sticking phase when the horizontal inertial force is below the instantaneous friction threshold. Slip occurs once the inertial force exceeds this threshold. The stepwise displacement response therefore results from periodic crossings of the friction threshold.

Figure 3 shows the motion of the system at four key instants during one motor revolution, captured by the high-speed camera. From the latter half of the previous cycle to point a in the current cycle, the system moves downward and stores elastic potential energy. At this time, the horizontal excitation is less than the instantaneous friction threshold, and the system tends to remain stationary. During the ab and bc stages, the system moves upward, releases elastic potential energy, and rapidly advances a short distance. It then stops at point d. The four image states correspond to the characteristic points in both the displacement curve in Figure 2(b) and the force curve in Figure 2(c). This correspondence shows that one motor revolution produces one stick–slip cycle. It can be concluded from the above analysis that the forward locomotion of the system results from the combined action of inertial and elastic forces. Due to the effect of the soft legs, a phase difference exists between the vertical inertial force and the elastic force. This phase difference further demonstrates the coupling phenomenon among the forces acting on the system.

To further simplify the dynamic equations, several dimensionless and new parameters are introduced. The dynamic equations are then rewritten as follows.

$$\begin{aligned}&\ddot{x}-\alpha A_e\ddot{\theta}\cos(\omega t-\theta)-\\&\alpha A_e(\omega-\dot{\theta})^2\sin(\omega t-\theta)=2\mu(p^2y+\eta^2\dot{y}),\end{aligned}\tag{4}$$

$$\begin{aligned}&\ddot{y}+\alpha A_e\ddot{\theta}\sin(\omega t-\theta)-\\&\alpha A_e(\omega-\dot{\theta})^2\cos(\omega t-\theta)+g+2p^2y+2\eta^2\dot{y}=0,\end{aligned}\tag{5}$$

$$\begin{aligned}&\ddot{\theta}-\frac{\beta}{A_e}\ddot{x}\cos(\omega t-\theta)+\frac{\beta}{A_e}\ddot{y}\sin(\omega t-\theta)+\\&\frac{\beta}{A_e}g\sin(\omega t-\theta)+\frac{1}{4}p^2\varepsilon^2\frac{\beta}{\alpha}\sin 2\theta+\\&\frac{1}{4}\eta^2\varepsilon^2\frac{\beta}{\alpha}\dot{\theta}(\cos 2\theta+1)=-2y\mu\left(\frac{p^2\beta}{A_e^2\alpha}y+\frac{\eta^2\beta}{A_e^2\alpha}\dot{y}\right),\end{aligned}\tag{6}$$

where $\alpha=\frac{m_e}{M}$, $\beta=\frac{m_eA_e^2}{I}$, $\varepsilon=\frac{l_0}{A_e}$, $p=\sqrt{\frac{k}{M}}$, $\eta=\sqrt{\frac{c}{M}}$, $M=2m+m_0+m_e$, $I=\frac{ml_0^2}{2}+\frac{m_0l_0^2}{12}+m_eA_e^2$.

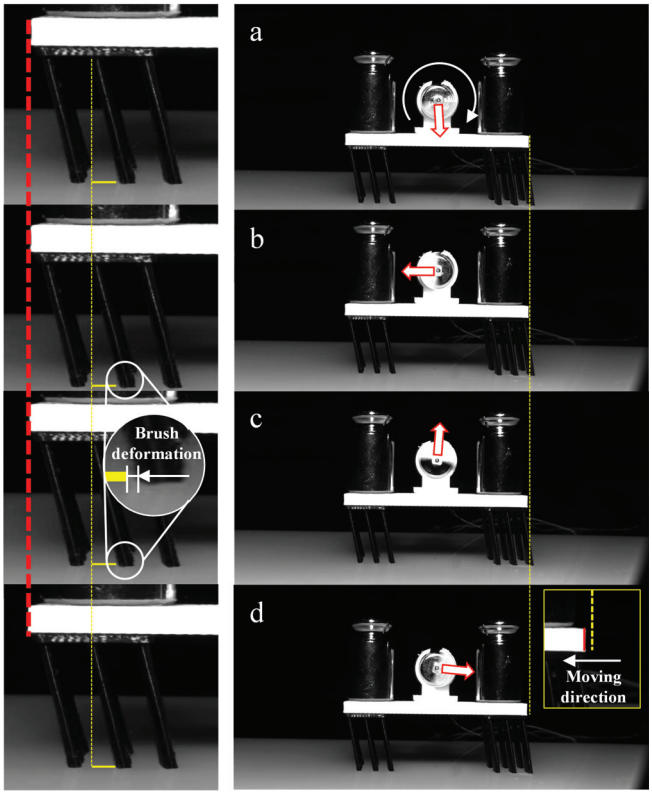


FIG. 3: Motion decomposition within one motor revolution captured by high-speed imaging. Multimedia 2 available online.

As the rotational speed of the eccentric rotor increases, the system transitions from a stationary state to a forward locomotion state. The frequency at which this transition occurs is called the critical frequency in this letter, denoted as ω_c . Near the onset of locomotion, the mean forward displacement, velocity, and acceleration vanish, allowing the horizontal equation to be reduced to a quasi-static balance between eccentric inertial forcing and the friction threshold. Meanwhile, it is assumed that both soft legs of the system remain in contact with the ground at this stage and that no jumping state exists. For the heave and pitch degrees of freedom, strong coupling appears between them. In the following analysis, the stiffness of pitch motion is greater than that of heave motion. Therefore, the pitch degree of freedom is neglected. Based on the above assumption, the following implicit critical equation is obtained:

$$\mu^2 g^2 = (\alpha A_e \omega_c^2)^2 \left\{ \left(1 + \frac{2\mu\omega_c^3\eta^2}{\Delta_{p_c}}\right)^2 + \left(\frac{2\mu}{\Delta_{p_c}}\left[p^2(2p^2-\omega_c^2)+2\eta^4\omega_c^2\right]\right)^2 \right\}, \tag{7}$$

where $\Delta_{p_c} = (2p^2-\omega_c^2)^2 + (2\eta^2\omega_c)^2$. This equation provides an implicit onset criterion for the transition between stationary and moving states. The criterion links the start-up boundary to eccentric inertial forcing, frictional resistance, and the heave response of the soft-legged system. The above assumption has been verified for the systems represented by this letter. The detailed derivation of the implicit critical equation together with the proof of these assumptions is given in Appendix D.

TABLE II: Parameters that reveal more complete regularities

Parameter	Value	Parameter	Value
α	0.07407	μ	0.1
β	0.00368	$A_e(\mathrm{m})$	0.1
ε	10	$g(\mathrm{m/s^2})$	9.81
η	0.43035	$M(\mathrm{kg})$	1

Through parametric analysis of the system, the parameters listed in Table II are obtained. With these parameters, the locomotion behaviors exhibited by the system are more diverse and pronounced than those obtained with the parameters listed in Table I. Therefore, the parameters listed in Table II are substituted into the dynamic equations for further investigation. By setting different values of ω and k, the system is found to exhibit five distinct locomotion states. Among them, the four dominant states are the stationary state, the slow-forward state, the intermittent state, and the high-speed forward state. Notably, a new mixed state appears between the stationary and locomotion states, namely the intermittent state. As shown in Figure 4(c), the system periodically alternates between stationary and moving in this state. When the time domain is further zoomed in, the motion curve is also found to consist of multiple step-like segments. This indicates that the system exhibits a "quasi-fractal" phenomenon of stick-slip motion in this state.

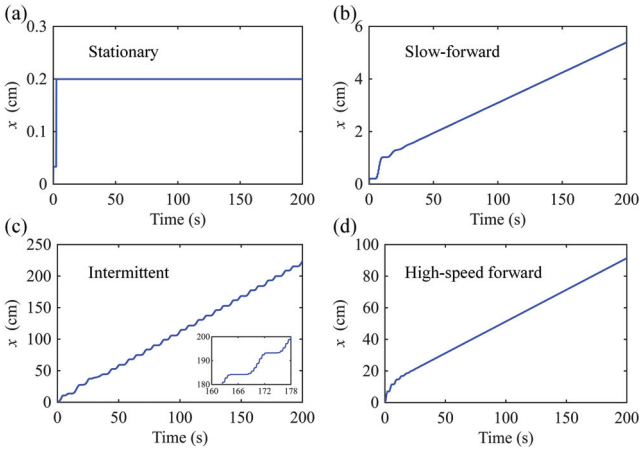


FIG. 4: Representative horizontal displacement responses for four locomotion states: stationary, slow-forward, intermittent, and high-speed forward. The inset highlights the local stepwise stick–slip motion in the intermittent state.

To more intuitively show the relationship between locomotion states and ω and k, the contour map in Figure 5 is plotted. Two special protruding peaks can be observed in the map. This motivates consideration of the effect of the system's natural frequencies. Analysis reveals that the system has a heave

natural frequency and a pitch natural frequency, denoted as

$$\omega_h = \sqrt{\frac{2k}{2m+m_0+m_e}} = \sqrt{2}p$$

and

$$\omega_p = \sqrt{\frac{6kl_0^2}{6ml_0^2+m_0l_0^2+12m_eA_e^2}}$$

respectively (see Appendix E for the derivation). The two natural frequency curves are plotted on the map. It is found that the red curve (heave natural frequency) and the cyan curve (pitch natural frequency) pass exactly through the middle of the two peaks. Moreover, the intermittent state with the "quasi-fractal" phenomenon appears precisely around the heave natural frequency curve, as shown in Figure 5. This demonstrates that resonance regulates the locomotion states of the system.

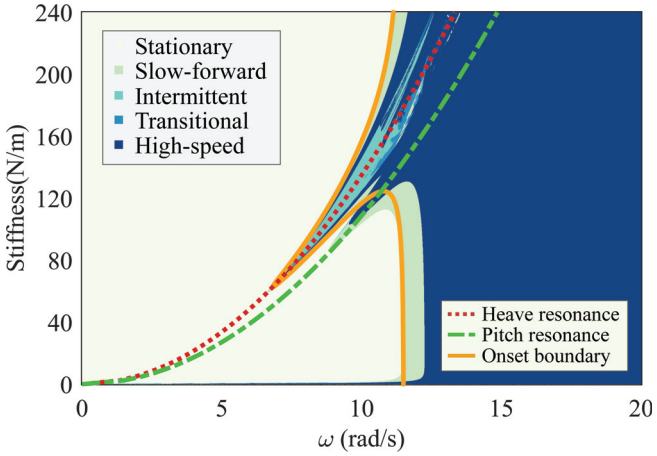


FIG. 5: Locomotion state map with heave/pitch resonance curves and the onset boundary.

Furthermore, the implicit start-up critical equation represented by (7) is plotted as a yellow curve in Figure 5. The curve effectively separates the static and dynamic states of the system. This not only proves the validity of the start-up critical equation but also reveals the diverse locomotion states that metastable systems near the critical curve may exhibit.

In summary, through theoretical modeling, numerical simulation, and experimental validation, this letter demonstrates that the proposed theoretical dynamic model of the dual-soft-legged vibratory robot can reflect the locomotion and mechanical behavior of the actual model to a certain extent. The results show that by changing the soft-leg stiffness and motor excitation frequency, the robot exhibits multiple locomotion modes based on the stick-slip effect, such as the stationary state, the intermittent state, and the high-speed forward state. In addition, the plots demonstrate the regulation of robot locomotion states by resonance. The locomotion criterion equation for the simplified model is also proposed. These results are of significant reference value for advancing research on robots with stick-slip effects.

See the **supplementary material** for the derivation of the simplified dynamic equations, the numerical calculation flowchart, the experimental calibration of stiffness and friction, the implicit critical equation, and the uncoupled natural frequencies. Figures S1–S3 show the bio-inspired design, numerical flowchart, and experimental setup.

This work was supported by Beijing Natural Science Foundation (No.QY26111).

AUTHOR DECLARATIONS

Conflict of Interest

The authors have no conflicts to disclose.

Author Contributions

Jingyuan Zeng: Formal analysis (lead); Methodology (lead); Software (lead); Investigation (equal); Writing – original draft (lead); Visualization (support); Validation (equal); Writing – review & editing (equal). **Ke Huang**: Visualization (lead); Conceptualization (equal); Investigation (equal); Resources (equal); Validation (equal); Project administration (support); Writing – review & editing (equal). **Zitong Zeng**: Investigation (equal); Validation (equal); Resources (equal); Visualization (support); Writing – review & editing (equal). **Jiaying Zhang**: Project administration (lead); Supervision (lead); Conceptualization (equal); Writing – review & editing (equal).

DATA AVAILABILITY

The data that support the findings of this study are available from the corresponding authors upon request.

REFERENCES

[1]K. Autumn, Y. A. Liang, S. T. Hsieh, W. Zesch, W. P. Chan, T. W. Kenny, R. Fearing, and R. J. Full, *Nature* **405**(6787), 681 (2000).

[2]A. P. Russell, *J. Zool.* **176**(4), 437 (1975).

[3]R. Ruibal and V. Ernst, *J. Morphol.* **117**(3), 271 (1965).

[4]K. Autumn, M. Sitti, Y. A. Liang, A. M. Peattie, W. R. Hansen, S. Sponberg, T. W. Kenny, R. Fearing, J. N. Israelachvili, and R. J. Full, *Proc. Natl. Acad. Sci. U.S.A.* **99**(19), 12252 (2002).

[5]R. H. Plaut, *Int. J. Non-Linear Mech.* **76**(2), 56 (2015).

[6]L. I. van Griethuijsen and B. A. Trimmer, *Biol. Rev.* **89**(3), 656 (2014).

[7]C. Bäumer, R. Pirow, and R. J. Paul, *Physiol. Biochem. Zool.* **73**(1), 77 (2000).

[8]G. Huber, S. N. Gorb, N. Hosoda, R. Spolenak, and E. Arzt, *Acta Biomater.* **3**(4), 607 (2007).

[9]P. Ditsche, J. Michels, A. Kovalev, J. Koop, and S. Gorb, *J. R. Soc. Interface* **11**(92), 20130989 (2014).

[10]Y. Pang and T. Liu, *Prog. Mater. Sci.* **158**, 101647 (2026).

[11]Y. R. Guo, X. B. Wang, L. W. Zhang, X. Z. Zhou, S. T. Wang, L. Jiang, and H. W. Chen, *ACS Nano* **19**(10), 9684 (2025).

[12]Z. Wang, *ACS Nano* **12**(2), 1273 (2018).

[13]A. G. Gillies and R. S. Fearing, *Langmuir* **27**(18), 11278 (2011).

[14]J. A. Booth and R. Hensel, *Appl. Phys. Lett.* **119**(23), 230502 (2021).

[15]Y. Zhang, M. Wang, Y. Cheng, D. Zheng, and Y. Peng, *Appl. Phys. Lett.* **115**(13), 131904 (2019).

[16]S. Bai, Q. Xu, and Y. Qin, *Sci. Rep.* **3**, 1851 (2013).

[17]Y. Liu, Y. Qin, D. Yuan, and W. Yuan, *Tribol. Int.* **198**, 109837 (2024).

[18]T. Shiratori, J. Sakamoto, Y. Kanazawa, M. Suzuki, T. Takahashi, and S. Aoyagi, *Appl. Phys. Lett.* **123**(4), 041603 (2023).

[19]H. Zhang and B. Xu, *Appl. Phys. Lett.* **121**(21), 214104 (2022).

[20]Z. Ji, C. Yan, S. Ma, S. Gorb, X. Jia, B. Yu, X. Wang, and F. Zhou, *Tribol. Int.* **132**, 99 (2019).

[21]H. Hirakata, T. Nishihira, A. Yonezu, and K. Minoshima, *Tribol. Lett.* **44**(2), 259 (2011).

[22]Y. Han, H. Marvi, and M. Sitti, *2015 IEEE International Conference on Robotics and Automation (ICRA)* 3122 (2015).

[23]H. Marvi, Y. Han, and M. Sitti, *Appl. Phys. Lett.* **106**(5), 051602 (2015).

[24]Y. Yan, L. Shui, S. Liu, Z. Liu, and Y. Liu, *Soft Robot.* **9**(5), 981 (2022).

[25]J. Meng, J. Guo, and L. Shui, *Arch. Appl. Mech.* **94**(7), 1911 (2024).

[26]T. Barois, A. Boucherie, L. Tadrist, and H. Kelly, *Phys. Rev. Lett.* **133**(23), 238301 (2024).

[27]S. Iyobe, M. Shimizu, and T. Umedachi, *IEEE Robot. Autom. Lett.* **7**(2), 992 (2022).

[28]Y. Liu, Y. Qin, J. Xu, D. Yuan, X.-Q. Feng, and W. Yuan, *Appl. Phys. Lett.* **127**(4), 044101 (2025).

[29]A. Breki and M. Nosonovsky, *Appl. Phys. Lett.* **113**(24), 241602 (2018).

[30]E. Pennestri, V. Rossi, P. Salvini, and P. P. Valentini, *Nonlinear Dyn.* **83**(4), 1785 (2016).